BFMSense: WiFi sensing using beamforming feedback matrix

Enze Yi, Dan Wu, Jie Xiong, Fusang Zhang, Kai Niu, Wenwei Li, Daqing Zhang

BFMSense: WiFi Sensing Using Beamforming Feedback Matrix

Enze Yi [1], Dan Wu [1], Jie Xiong [2], Fusang Zhang [3,4], Kai Niu [5], Wenwei Li [1], Daqing Zhang [1,6]
[1] *Peking University,* [2] *University of Massachusetts Amherst,*
[3] *Institute of Software, Chinese Academy of Sciences,* [4] *University of Chinese Academy of Sciences,*
[5] *Beijing Xiaomi Mobile Software Company Ltd.,* [6] *Institut Polytechnique de Paris*

Abstract

WiFi-based contactless sensing has attracted a tremendous amount of attention due to its pervasiveness, low-cost, and non-intrusiveness to users. Existing systems mainly leverage channel state information (CSI) for sensing. However, CSI can only be extracted from very few commodity WiFi devices through driver hacking, severely limiting the adoption of WiFi sensing in real life. We observe a new opportunity that a large range of new-generation WiFi cards can report another piece of information, i.e., beamforming feedback matrix (BFM). In this paper, we propose to leverage this new BFM information for WiFi sensing. Through establishing the relationship between BFM and CSI, we lay the theoretical foundations for BFM-based WiFi sensing for the first time. We show that through careful signal processing, BFM can be utilized for fine-grained sensing. We showcase the sensing capability of BFM using two representative sensing applications, i.e., respiration sensing and human trajectory tracking. Comprehensive experiments show that BFM-based WiFi sensing can achieve highly accurate sensing performance on a large range of new-generation WiFi devices from various manufacturers, moving WiFi sensing one big step towards real-life adoption.

1 Introduction

In recent years, WiFi-based contactless sensing has attracted lots of attention from both academia and industry owing to the pervasive deployment of WiFi infrastructure in indoor environments. A large number of sensing applications have been successfully demonstrated with WiFi sensing such as passive localization [25, 36], fall detection [42, 46], gesture recognition [38, 40], activity recognition [33, 45, 56], and vital sign monitoring [61, 67]. The basic principle of WiFi sensing is that WiFi signals vary with target movement and we can thus extract target movement information through analyzing the induced signal variations.

Early research on wireless sensing was mostly based on software-defined radio (SDR) platforms such as WARP [31] and USRP [4, 35]. On these platforms, raw WiFi signal samples can be obtained at very high rates for sensing purposes. Though promising, there is actually a huge gap between SDR platform and commodity hardware. Commodity WiFi hardware can only report the processed low-frequency received-signal-strength-indicator (RSSI) samples. While RSSI can still be utilized for sensing [48, 59], it is relatively coarse and only contains signal amplitude information. Researchers further proposed to use channel state information (CSI) which contains both signal amplitude and phase information for sensing [44, 50, 57, 61]. Although CSI contains finer-grained information, one critical issue hindering the wide adoption of CSI-based sensing is that CSI can only be extracted from few commodity WiFi cards such as Intel 5300 [17] and Atheros WiFi cards [55] through driver hacking.

In the last few years, we observed an exciting trend which may be leveraged to address the above issue, i.e., with the popularity of IEEE 802.11ac standard [47], more and more commodity WiFi devices now adopt MU-MIMO (multi-user multiple input and multiple output) technology [8, 23]. New generation WiFi cards from Qualcomm, Broadcom, MediaTek, and others supporting MU-MIMO have become increasingly dominant on the market. For example, Broadcom BCM4366 and BCM43684 chips are used in ASUS RT-AC86U [22] and TP-LINK XDR6060 WiFi routers [9]. Qualcomm QCA9886 and QCA9984 are used in Linksys EA8300 and Netgear X4S R7800 [6].

The key feature of MU-MIMO is enabling a single access point (AP) to simultaneously transmit to multiple stations. To enable MU-MIMO, each WiFi station needs to measure the channel and send the channel measurement, i.e., beamforming feedback matrix (BFM) to the access point (AP). As BFM also contains channel information, BFM may also be utilized for sensing like CSI. There are two obvious advantages of leveraging BFM for sensing.

- BFM is transmitted without encryption.
- BFM is protocol-compliant, and it can be extracted from all new-generation MU-MIMO-enabled WiFi devices without a need of special firmware or driver.

Though promising, we quickly realize the key challenge of

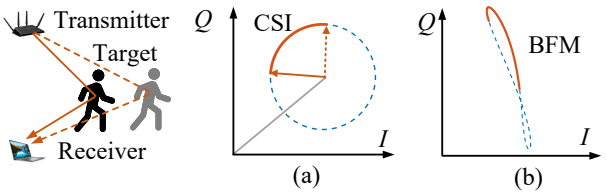

Figure 1: (a) The trajectory (i.e., a circle) of ideal CSI on the complex plane. (b) For BFM, the signal variation does not form a circle on the complex plane.

utilizing BFM for sensing. To reduce the transmission overhead, BFM does not contain raw channel amplitude/phase information like CSI. Instead, BFM only contains the SVD-decomposed component of the channel required for beamforming. That is to say, BFM only contains partial information of CSI. Hence, to utilize BFM for sensing, the key questions we need to answer are:

- As BFM only contains partial information of the channel (i.e., CSI), can BFM still be used for sensing?
- Even if BFM can be utilized for sensing, will BFM be able to achieve comparable performance to that achieved with CSI?
- A large number of sensing models based on CSI have been developed. Are those sensing models and algorithms designed for CSI still applicable to BFM sensing?

This paper aims to answer these questions. Specifically, this paper targets to reveal the relationship between CSI and BFM and understand the basic principle of BFM sensing. These theoretical analyses lay a foundation for WiFi sensing on new-generation cards. Also, we aim to explore the sensing capability of BFM in real-world environments.

After some initial studies, we find that BFM does change with target movement. However, different from CSI, the quantitative relationship between BFM and target motions does not exist. One key property utilized to obtain quantitative measurement (e.g., target movement distance) in CSI-based sensing is that for small displacements, target motions only induce a signal phase change and the signal amplitude remains a constant [41, 44]. Thus, the signal variation on the complex I-Q plane forms a circle as shown in Figure 1(a). We can therefore use the amount of phase rotation to calculate fine-grained target displacement. However, for BFM, the signal variation does not form a circle anymore as shown in Figure 1(b), and that quantitative relationship disappears.

Upon deeper investigation, we find that this is because each time when BFM is calculated, the BFM is scaled by a time-varying coefficient. To address this issue, we leverage one key observation, i.e., although the BFM is scaled by a time-varying coefficient, the same coefficient is applied to all the BFM elements. Based on this observation, we define a new measurement, i.e., BFM-ratio by taking the ratio between two BFM elements[1] for sensing. We demonstrate that theoretically, the sensing performance using BFM-ratio can approach that using CSI. We show that BFM-ratio can be used to not just detect target motions but also quantitatively sense the target movement distance. The main contributions of this paper are summarized below.

- Through theoretically deriving the mathematical relationship between BFM and CSI, we propose a BFM-ratio model to make fine-grained BFM sensing possible for the first time. We believe the widely available BFM data can move WiFi sensing one big step forward towards wider adoption compared to traditional CSI sensing.
- We explore the sensing capability of BFM both theoretically and experimentally to lay a foundation for WiFi sensing with new-generation cards.
- We showcase BFM sensing using two representative sensing applications, i.e., respiration monitoring and human trajectory tracking. The extensive evaluation demonstrates the feasibility of BFM sensing on a large range of new-generation WiFi cards.

2 Background

Before introducing BFM-based sensing, we briefly introduce the background of WiFi CSI and BFM.

2.1 CSI Primer

In a communication system, the channel state describes how a signal propagates through a wireless channel. For a signal X to be transmitted and Y to be received, the signal propagation characteristics are represented by CSI h as $Y = hX + n$, where n is the channel-induced noise. In an indoor environment as shown in Figure 2(a), WiFi signals travel from a transmitter (Tx) to a receiver (Rx) through multiple paths. As the signal received by the receiver is a superposition of signals propagated along multiple paths, mathematically the CSI with frequency f for a pair of transmitter-receiver at time t can be expressed as:

$$h(f,t) = \sum_{i=1}^{K} A_i e^{-j\frac{2\pi f d_i(t)}{c}}, \quad (1)$$

where A_i and $d_i(t)$ are the signal amplitude attenuation and the i-th signal path length, respectively. K is the total number of propagation paths and c is the speed of light.

Among the propagation paths, some are static and do not change within a short period of time, such as the paths reflected from static objects in the environment. Other paths affected by moving objects (e.g., human motions) are dynamic, and the lengths of these paths change with human motions. CSI can then be denoted as the summation of the static component and the dynamic component:

$$h(f,t) = h_s(f) + h_d(f,t) = h_s(f) + A_d e^{-j\frac{2\pi f d(t)}{c}}, \quad (2)$$

[1]The number of elements equals to the number of antennas at the WiFi AP. For example, when there are four antennas at the AP side, there are four BFM elements.

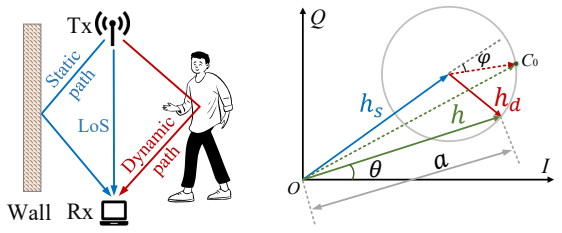

(a) (b)

Figure 2: (a) The human motion causes variation of the reflection path. (b) The ideal CSI on the complex I-Q plane. C_0 indicates the initial point of CSI.

where $h_s(f)$ and $h_d(f,t)$ are the static component and the dynamic component, respectively. $d(t)$ is the length of the dynamic path. According to Equation (2), when the change of dynamic path length is one wavelength, the dynamic component vector $h_d(f,t)$ rotates 360 degrees on the I-Q plane as shown in Figure 2(b).

We denote $a(f,t)$ and $\theta(f,t)$ as the amplitude and phase of CSI $h(f,t)$, i.e., $h(f,t) = a(f,t)e^{j\theta(f,t)}$. For an ideal CSI, its amplitude and phase can be calculated as [41, 61]:

$$a(f,t)^2 = |h_s(f)|^2 + A_d^2 + 2A_d|h_s(f)|\cos\left(\frac{2\pi f \Delta d(t)}{c} + \varphi(f)\right), \tag{3}$$

$$\theta(f,t) \approx \angle h_s(f) - \frac{A_d \sin\left(\frac{2\pi f \Delta d(t)}{c} + \varphi(f)\right)}{a(f,t)}, \tag{4}$$

respectively, where $\Delta d(t)$ is the path length change. $\varphi(f) = \pi + \angle h_s(f) + \frac{2\pi f d_0}{c}$ represents the supplementary angle of the initial phase difference between the dynamic component and the static component, where d_0 is the initial dynamic path length. Equation (3) and Equation (4) show that for one wavelength change of Δd, both signal amplitude and phase change for one cycle.

Given M antennas at the transmitter and N antennas at the receiver, CSI is a $N \times M$ dimensional complex-valued matrix $H(f,t)$ for one subcarrier at time t. $h_{p,q}(f,t)$ denotes the channel state from the q-th antenna of the transmitter to the p-th antenna of the receiver. Specifically, $h_{p,q}(f,t)$ can be expressed as $a_{p,q}(f,t)e^{j\theta_{p,q}(f,t)}$, where the expression of $a_{p,q}$ and $\theta_{p,q}(f,t)$ are presented in Equation (3) and Equation (4) respectively.

Due to unsynchronized clocks between the WiFi transmitter and receiver, the phase of actual CSI (denoted as $\widehat{H}(f,t)$) contains a time-varying random phase offset $\varepsilon(f,t)$. The (p,q) element of $\widehat{H}(f,t)$ can then be expressed as:

$$[\widehat{H}(f,t)]_{p,q} = a_{p,q}(f,t)e^{j\left(\theta_{p,q}(f,t)+\varepsilon(f,t)\right)}, \tag{5}$$

where $[\cdot]_{p,q}$ represents the element of the p-th row and q-th column of a matrix. For the sake of brevity, f and t will be omitted in the rest of formulas.

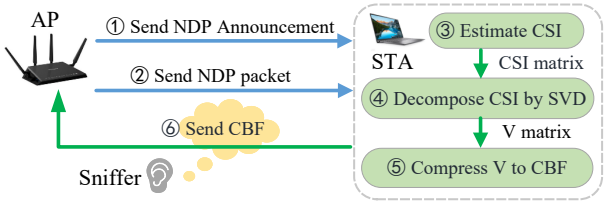

Figure 3: The sounding procedure for MU-MIMO transmissions (IEEE 802.11ac).

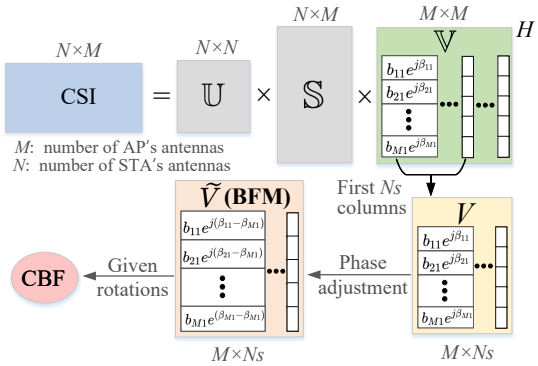

Figure 4: The data flow from CSI to CBF.

2.2 BFM primer

Beamforming feedback matrix (BFM) is another type of information in WiFi that is capable of depicting wireless channels. BFM is mainly used to enable MU-MIMO transmission, which is one key feature of the 802.11ac WiFi standard.

To support MU-MIMO, WiFi AP needs to know the channel information between AP and all the stations (STAs). The channel information (BFM) is sent from STAs to AP in a compressed form, i.e., compressed beamforming feedback (CBF). With the BFM information, AP can then steer the beams towards the desired directions by adjusting the weight of each antenna's transmitted signal.

Although BFM also depicts wireless channel, it is different from CSI. This is because the AP only requires information to calculate the antenna weights for beamforming, as opposed to the entire channel state information. In order to reduce the high transmission overhead of sending the entire channel state, STA decomposes the measured CSI using singular value decomposition (SVD). BFM is then extracted from the right singular matrix and further compressed as CBF, which is subsequently sent back to AP.

Taking an AP and a STA as an example, the detailed procedure is shown in Figure 3. It contains the following steps:

- Step 1: AP broadcasts a Null Data Packet Announcement (NDPA) frame to inform STAs in the same WLAN that the sounding procedure starts.
- Step 2: AP broadcasts a NDP packet to STAs for CSI estimation.
- Step 3: STA estimates CSI as a $N \times M$ matrix ($\widehat{H}$) for each subcarrier, where M and N are the numbers of transmitting and receiving antennas, respectively.

- Step 4: STA decomposes $\widehat{H}$ using SVD operation:

$$\widehat{H} = \mathbb{U}\mathbb{S}\mathbb{V}^H, \tag{6}$$

where $\mathbb{S}$ is a diagonal matrix whose diagonal elements σ_k ($k = 1, \cdots, \min(N,M)$) are real singular values. $\mathbb{U}$ and $\mathbb{V}$ are left and right singular matrices which are unitary matrices containing complex-valued elements with a size of $N \times N$ and $M \times M$, respectively. $\mathbb{V}^H$ indicates the Hermitian transpose of $\mathbb{V}$. Mathematically, we have

$$\sum_{p=1}^{M} b_{p,q}^2 = 1, \tag{7}$$

where $b_{p,q}$ is the amplitude of the (p,q) element in $\mathbb{V}$, and $q = 1, \cdots, M$.
- Step 5: STA extracts the first N_s singular vectors out of $\mathbb{V}$ to construct a new matrix V for beamforming, where N_s is the number of spatial streams which is no more than $\min(N,M)$. Before compression, a phase adjustment step is applied to each column. Specifically, the phase of each column element of V is subtracted by the phase of the last element in the column of V, and a phase-adjusted matrix $\widetilde{V}$ is obtained, which is equivalent to V for beamforming [23, 34]. $\widetilde{V}$ is known as beamforming feedback matrix (BFM). Then, $\widetilde{V}$ is further compressed by applying Givens Rotation to obtain CBF. Figure 4 shows the detailed conversion procedure from CSI to CBF. For the detailed compression algorithm, please refer to IEEE 802.11-2016 [14].
- Step 6: STA sends the CBF back to AP. Based on IEEE standard [14], CBF is transmitted without encryption.

When there are multiple STAs, they send CBF to AP one by one. CBF is transmitted without encryption and can be overheard by any third party in the environment.

3 Understanding the relationship between BFM and human motion

As BFM is partial information of CSI, we proceed in Subsection 3.1 to establish the mathematical connection between BFM and CSI. Based on the established connection, we derive the relationship between BFM and human motion, and analyze the properties of BFM for sensing in Subsection 3.2.

3.1 The mathematical connection between CSI and BFM

The data processing procedure from CSI to BFM involves the decomposition of CSI using SVD to obtain the matrix V. Subsequently, BFM is derived by applying simple phase adjustment to the column vector of V. In light of this, our effort is directed towards understanding the mathematical relationship between V and CSI, following which we deduce the relationship between BFM and CSI, utilizing V as an intermediary.

3.1.1 Relationship between CSI and V

In this section, we study the mathematical relationship between V and CSI. We construct the following equation:

$$\widehat{H}^H\widehat{H} = \mathbb{V}\mathbb{S}^H\mathbb{U}^H\mathbb{U}\mathbb{S}\mathbb{V}^H = \mathbb{V}\mathbb{S}^H\mathbb{S}\mathbb{V}^H. \tag{8}$$

Due to the fact that $\mathbb{U}$ is a unitary matrix, we have $\mathbb{U}^H\mathbb{U} = E$, where E is an identity matrix. Thus the impact of $\mathbb{U}$ can be eliminated by Equation (8).

We assume that AP has M antennas, STA has N antennas, and $M \geq N$. We first substitute Equation (5) into the left side of Equation (8) and obtain a $M \times M$ matrix and the (p,q) element can be written as:

$$[\widehat{H}^H\widehat{H}]_{p,q} = \sum_{k=1}^{N} a_{k,p}a_{k,q}e^{j(\theta_{k,q}-\theta_{k,p})}, \tag{9}$$

where $p, q = 1, 2, \cdots, M$. p and q are the antenna index at the AP while k is the antenna index at the STA. As two antennas at the AP share the same phase offset, the offset is canceled out in $\theta_{k,q} - \theta_{k,p}$.

For the right side of Equation (8), if the diagonal matrix S is marked as $\text{diag}(\sigma_1, \cdots, \sigma_N)$, and the amplitude and phase of (p,q) element in $\mathbb{V}$ are denoted as $b_{p,q}$ and $\beta_{p,q}$ respectively, the (p,q) element of $\mathbb{V}\mathbb{S}^H\mathbb{S}\mathbb{V}^H$ can be expressed as:

$$[\mathbb{V}\mathbb{S}^H\mathbb{S}\mathbb{V}^H]_{p,q} = \sum_{k=1}^{N} \sigma_k^2 b_{p,k}b_{q,k}e^{j(\beta_{p,k}-\beta_{q,k})}. \tag{10}$$

According to Equation (8), the items represented by Equation (9) and Equation (10) are equal. Without loss of generality, we assume there is only one antenna at the STA, that is, $N = N_s = 1$, and V is generated using the first singular vector of the $\mathbb{V}$ matrix. We thus have:

$$\sigma_1^2 b_{p,1}b_{q,1}e^{j(\beta_{p,1}-\beta_{q,1})} = a_{1,p}a_{1,q}e^{j(\theta_{1,q}-\theta_{1,p})}. \tag{11}$$

Next, we discuss the relationship between the amplitude and phase of V and the CSI amplitude and phase.

Amplitude of V. We let $p = q$ and Equation (11) is simplified as $\sigma_1^2 b_{p,1}^2 = a_{1,p}^2$. Then, the amplitude of elements in V can be obtained as:

$$b_{p,1} = \frac{a_{1,p}}{\sigma_1}. \tag{12}$$

The amplitude of the p-th element in V is equal to a scaled amplitude of CSI between the p-th antenna of AP and STA, where the scaling factor is the singular value. Based on Equation (7), we can further derive the singular value σ_1^2 as follows:

$$\sigma_1^2 = \sum_{p=1}^{M} a_{1,p}^2. \tag{13}$$

Equation (13) indicates that σ_1^2 is the sum of squares of the CSI amplitudes between all the AP's antennas and STA's

antenna. It should be noted that, under target motions, CSI amplitude varies and σ_1 is thus time varying.

Phase of V. If $p \neq q$ in Equation (11), we can obtain the relationship between the phase difference of V and phase difference of CSI as follows:

$$\beta_{p,1} - \beta_{q,1} = \theta_{1,q} - \theta_{1,p}. \tag{14}$$

Equation (14) shows that the phase difference between the p-th and q-th elements in V is equal to the phase difference between the CSIs of AP's q-th, p-th antenna and STA.

3.1.2 From V to BFM $\widetilde{V}$

As AP adjusts the phase of multiple transmitted signals on multiple antennas simultaneously based on the feedback, the phase difference matters rather than the absolute phase. To effectively compress V and reduce the amount of feedback, a phase adjustment is made first. Specifically, the phase of each element in V is subtracted by the phase of the last element in V to obtain BFM $\widetilde{V}$. The element in $\widetilde{V}$ can be expressed as follows:

$$[\widetilde{V}]_{p,1} = b_{p,1} e^{j(\beta_{p,1} - \beta_{M,1})} = \frac{a_{1,p}}{\sigma_1} e^{j(\theta_{1,M} - \theta_{1,p})}. \tag{15}$$

The amplitude of $\widetilde{V}$ is the same as that of V. Since the amount of phase adjustment is not fed back to AP, we are unable to reconstruct V but can only reconstruct BFM $\widetilde{V}$.

To sum up, we establish the mathematical relationship between BFM and CSI as follows:

- The amplitude of the p-th element in BFM is equal to the amplitude of CSI between the p-th antenna of AP and STA scaled by the singular value.
- The phase of the p-th element in the BFM is equal to the CSI phase difference between AP-last antenna-STA and AP-p-th antenna-STA.

Noted that in the above derivation, the AP is considered to have multiple antennas, and the STA is considered to have one antenna. So the BFM in this case is actually a 1-D vector but not a 2-D matrix. Therefore, the "element" in the derivation indicates a single element of a vector.

3.2 Sensing Target Motion using BFM

In the previous section, we establish the mathematical expression of BFM amplitude and phase. Based on it, we can analyze the characteristics when we use BFM amplitude and phase for sensing. We take respiration sensing as an example to illustrate the concept.

3.2.1 Sensing motion using BFM amplitude

Based on the mathematical relationship between the amplitude ($|\widetilde{V}|$) of BFM and that of CSI presented in Equation (12) and the relationship between the CSI amplitude and length change of the dynamic path (Δd) given in Equation (3), the mathematical relationship between $|\widetilde{V}|$ and Δd can be obtained as follows:

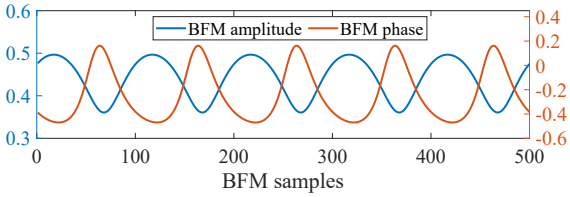

Figure 5: The simulated variation of BFM amplitude ($|\widetilde{V}|$) and phase ($\angle\widetilde{V}$) when dynamic path length changes by 5 wavelengths.

$$|[\widetilde{V}]_{p,1}|^2 = \frac{a_{1,p}^2}{\sigma_1^2} = \frac{\mathcal{F}_p + \mathcal{G}_p \cos\left(\frac{2\pi f \Delta d_{1,p}}{c} + \varphi_{1,p}\right)}{\sum_{m=1}^{M}\left(\mathcal{F}_m + \mathcal{G}_m \cos\left(\frac{2\pi f \Delta d_{1,m}}{c} + \varphi_{1,m}\right)\right)}, \tag{16}$$

where $\mathcal{F}_p = |h_{s_{1,p}}|^2 + A_{d_{1,p}}^2$, and $\mathcal{G}_p = 2A_{d_{1,p}}|h_{s_{1,p}}|$. Since the target is usually far away from the transceiver, we can assume that the dynamic path changes (Δd) at different antennas are equal, i.e., $\Delta d_{1,1} = \Delta d_{1,2} = \cdots = \Delta d_{1,M}$. In this case, we can regard $|[\widetilde{V}]_{p,1}|$ as a function $|[\widetilde{V}]_{p,1}|(\Delta d_{1,p})$ with $\Delta d_{1,p}$ as the variable because other parameters in Equation (16) are constants. Then we can obtain $|[\widetilde{V}]_{p,1}|(\Delta d_{1,p}) = |[\widetilde{V}]_{p,1}|(\Delta d_{1,p} + n\lambda)$, where n is an integer. Therefore, each time the dynamic path length changes by one wavelength, the BFM amplitude varies by one cycle as shown in Figure 5.

3.2.2 Sensing motion using BFM phase

Based on the mathematical relationship between the phase ($\angle\widetilde{V}$) of BFM and that of CSI given in Equation (15) and the relationship between CSI phase and length change of dynamic path Δd given in Equation (4), the mathematical expression between $\angle\widetilde{V}$ and Δd can be obtained as follows:

$$\begin{aligned}\angle[\widetilde{V}]_{p,1} =& \theta_{1,M} - \theta_{1,p} = \angle h_{s_{1,M}} - \angle h_{s_{1p}} \\ &+ \frac{A_{d_{1,p}} \sin\left(\frac{2\pi\Delta d_{1,p}}{\lambda} + \varphi_{1,p}(f)\right)}{a_{1,p}} \\ &- \frac{A_{d_{1,M}} \sin\left(\frac{2\pi\Delta d_{1,M}}{\lambda} + \varphi_{1,M}(f)\right)}{a_{1,M}}.\end{aligned} \tag{17}$$

Similar to BFM amplitude, BFM phase $\angle\widetilde{V}_{p,1}$ can be regarded as a function $\angle\widetilde{V}_{p,1}(\Delta d_{1,p})$ with $\Delta d_{1,p}$ as the variable. Then we can obtain $\angle[\widetilde{V}]_{p,1}(\Delta d_{1,p}) = \angle[\widetilde{V}]_{p,1}(\Delta d_{1,p} + n\lambda)$, where n is an integer. Therefore, each time the dynamic path length changes by one wavelength, the BFM phase varies by one cycle as shown in Figure 5.

3.2.3 Sensing using both BFM amplitude and phase

We compare the differences between BFM and CSI patterns on the complex plane using simulation. By setting the change of dynamic reflection path length to one wavelength in all the

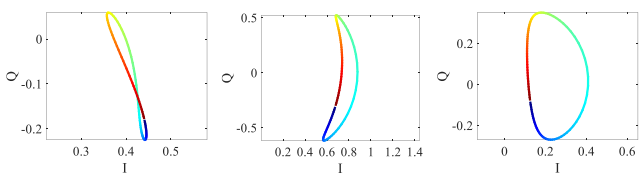

Figure 6: Three examples of one single element of BFM on the complex plane when the dynamic path length increases by a wavelength (the blue color indicates the starting point).

simulations, we obtain various BFM patterns on the complex plane under different settings as shown in Figure 6. Different from the trajectory of CSI which is a circle, the trajectory of BFM is not a circle but there exist a variety of patterns. This difference is due to varying BFM amplitude and phase detailed as below:

- Compared to CSI, the amplitude of BFM is multiplied by a scaling factor. Since this factor is affected by the signal amplitude of all antennas, it is a time-varying variable, causing the BFM amplitude to vary.
- The phase of BFM element is the phase difference of two antennas. It varies with target movement and the coupling between phase difference and signal amplitude is much weaker than that between CSI phase and signal amplitude.

Due to the clear difference between BFM and CSI patterns on the complex plane, many existing CSI-based sensing models and methods cannot be directly applied for BFM sensing.

3.2.4 Case study

We take respiration monitoring as an example to analyze the characteristics of BFM sensing. Respiration induces repetitive small motions. During natural breath, the movement of the chest is about 5mm [29], and the corresponding dynamic path length varies by about one-sixth of a wavelength for 5 GHz WiFi signals. When the reflection path length changes by one wavelength, the BFM amplitude varies for one complete cycle. As respiration causes a change smaller than a complete wavelength, the BFM amplitude change induced by respiration is a fragment of the complete curve. The curve fragments differ when a subject is at different positions, resulting in different amounts of amplitude variations as shown in Figure 7(b). At some positions, the BFM amplitude variations caused by respiration are large and can be easily detected. We call such positions 'good positions' for sensing. Those positions with small amplitude variations can be buried by noise and they are called 'bad positions'.

Through the above example, we can see that the sensing performance using BFM amplitude varies across locations. Similarly, using the BFM phase alone also faces the same problem. This problem was also studied in a recent work [61]. In this work, the complementary property of CSI amplitude and phase on sensing capability is utilized to remove those

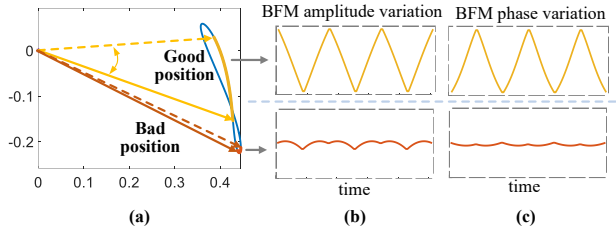

Figure 7: (a) At different initial positions, signal variations induced by respiration correspond to different BFM fragments.

'bad positions'. This is because a 'bad position' for CSI amplitude is a 'good position' for CSI phase, and vice versa.

Unfortunately, such an idea is not applicable in BFM-based sensing. Taking the BFM trajectory on the complex plane in Figure 7 as an example, we can see that at the 'bad' positions, both BFM amplitude and phase perform badly with small signal fluctuation. This is because the complementary property relies on the circular trajectory. As the BFM trajectory on the complex plane is no longer a circle, its amplitude and phase lose the complementary sensing capability.

In summary, the 'bad position' problem still exists when we employ BFM for sensing. Furthermore, conventional solutions such as employing the complementary property of phase and amplitude can not be applied on BFM sensing. In addition, because the quantitative relationship between BFM and target displacement is lost, BFM cannot be used to sense target displacement.

4 Motion Sensing with BFM-Ratio Metric

To address the 'bad position' issue and enable quantitative target displacement sensing, we propose a new metric named BFM-ratio and validate its benefits for sensing in this section.

4.1 BFM-Ratio Metric

As demonstrated in Section 3.2, the time-varying scaling factor in BFM amplitude and uncertain phase offset are the key reasons corrupting the mapping between BFM and target motion. To obtain the mapping, we need to eliminate the effect of the scaling factor on BFM amplitude and the phase offset on BFM phase. Fortunately, although the scaling factors keep changing over time, they are identical at different elements of the BFM matrix, as shown in Equation (12). We thus propose to leverage the ratio of two BFM elements to eliminate the effect of the scaling factor. Specifically, we call it BFM-ratio which can be expressed as:

$$\frac{\widetilde{V}_{1,p}}{\widetilde{V}_{1,q}} = \frac{\frac{a_{1,p}}{\sigma_1} e^{j(\theta_{1,M}-\theta_{1,p})}}{\frac{a_{1,q}}{\sigma_1} e^{j(\theta_{1,M}-\theta_{1,q})}} = \frac{a_{1,p}e^{-j\theta_{1,p}}}{a_{1,q}e^{-j\theta_{1,q}}} \tag{18}$$
$$= \frac{\overline{h_{s_{1,p}}} + A_{1,p}e^{j(\frac{2\pi\Delta d_{1,p}}{\lambda}+\varphi_{1,p})}}{\overline{h_{s_{1,q}}} + A_{1,q}e^{j(\frac{2\pi\Delta d_{1,q}}{\lambda}+\varphi_{1,q})}},$$

where $\overline{h_{s_{1,p}}}$ is the conjugate of $h_{s_{1,p}}$. For simplicity, we let $\mathcal{A}_p = \overline{h_{s_{1,p}}}$, $\mathcal{A}_q = \overline{h_{s_{1,q}}}$, $\mathcal{B}_p = A_{1,p}e^{j\varphi_{1,p}}$, and $\mathcal{B}_q = A_{1,q}e^{j\varphi_{1,q}}$.

When the person is far away from the transceivers, the difference between the two reflection path length variations can be regarded to be the same at two close-by antennas, that is $\Delta d_{1,p} \approx \Delta d_{1,q}$. Therefore, we let $\mathcal{Z}$ present $e^{j\frac{2\pi\Delta d_{1,p}}{\lambda}}$ and $e^{j\frac{2\pi\Delta d_{1,q}}{\lambda}}$. Then Equation (18) can be simplified as:

$$\frac{\widetilde{V}_{1,p}}{\widetilde{V}_{1,q}} = \frac{\mathcal{A}_p + \mathcal{B}_p\mathcal{Z}}{\mathcal{A}_q + \mathcal{B}_q\mathcal{Z}}, \tag{19}$$

where $\mathcal{A}_p$, $\mathcal{A}_q$, $\mathcal{B}_p$ and $\mathcal{B}_q$ can be regarded as complex constants when the target moves a small distance (e.g., chest displacement during respiration). $\mathcal{Z}$ represents a unit circle rotating counterclockwise when $\Delta d_{1,p}$ is increased by one wavelength. From Equation 19, we can see that the ratio of two BFM elements is in the form of the Möbius transformation [37] as long as $\mathcal{A}_p\mathcal{B}_q \neq \mathcal{A}_q\mathcal{B}_p$. One property of Möbius transformation is that it maps circles to circles [24]. For the unit circle of $\mathcal{Z}$, the BFM ratio keeps the shape of a circle on the complex plane [7]. That is to say, when the path length of the dynamic signal is changed by one wavelength, the BFM-ratio vector also experiences a phase rotation of 360 degrees on the I-Q plane. Based on this property, we can obtain the following properties of the BFM ratio for sensing:

1. BFM-ratio rotates a circle on the complex plane if the reflection path length is changed by one wavelength. The BFM-ratio rotates an arc on the complex plane if the reflection path length is changed by less than a wavelength.
2. When the magnitude of the static component of CSI is larger than that of the dynamic component of CSI ($|\mathcal{A}_q| > |\mathcal{B}_q|$), BFM ratio rotates counterclockwise as the length of the reflection path increases. Otherwise, it rotates clockwise. In most cases, the static path component (i.e., LoS path and reflection from static objects) is stronger than the reflection from the human body.

With the above properties, we successfully construct a mapping between BFM-ratio and the change in signal path length induced by motion, laying the foundation for BFM sensing.

4.2 Experiment Verification

We verify the above properties via benchmark experiments. We utilize a Netgear Nighthawk X4S R7800 WiFi AP as the transmitter and a Tenda U10 WiFi Dongle as the receiver. They are placed with a LoS distance of 2.4 m. The central frequency is set as 5.765 GHz, corresponding to a signal wavelength of 5.2 cm. To mimic a moving target, an iron plate was placed on a sliding track in the direction of the perpendicular bisector of the LoS path, as shown in Figure 8. We moved the iron plate to vary the reflection path length. When the dynamic path length changes by one wavelength, while the trajectory of BFM on the I-Q plane is not circular, the BFM ratio trajectory is a complete circle as shown in Figure 9(a). Notably, the BFM ratio rotated counterclockwise when the plate was moved away from the LoS path, and

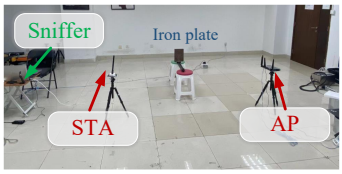

Figure 8: Experiment setting for model verification.

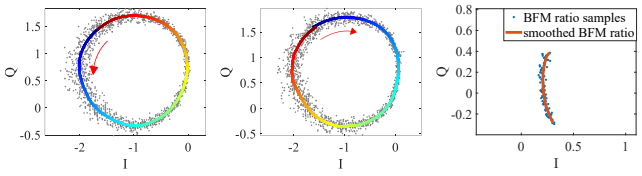

(a) (b) (c)

Figure 9: Trajectory of smoothed BFM ratio when the dynamic path length (a) increases by one wavelength (the blue color indicates the starting point), (b) decreases by one wavelength, and (c) changes by one-sixth of a wavelength.

clockwise when it approached the LoS path. We also control the starting position of the iron plate to make the length of the dynamic reflection path change by one-sixth of a wavelength, and the trajectory of the BFM ratio is shown in Figure 9(c). The radian of the BFM ratio trajectory is roughly 60 degrees, which well matches the theoretical value.

5 Case Study

As BFM ratio restores the quantitative mapping between signal variation and target motion, various sensing applications can be realized based on the BFM ratio. In this section, we employ two applications, i.e., micro-motion breath monitoring and macro-motion human walking tracking to demonstrate the sensing capability of BFM ratio.

5.1 Respiration Monitoring

BFM ratio can be used for reliable respiration monitoring without incurring the 'bad position' problem. We calculate the BFM ratio of each pair of elements in BFM and perform this operation on all the subcarriers. For example, when AP and STA have 4 antennas and 1 antenna respectively with 234 subcarriers, $234 \times C_4^2$ streams of BFM ratios can be obtained. Each BFM ratio stream can be further divided into amplitude and phase streams, and we can obtain a total of 2808 streams. We can now extract the respiration information by applying the principal component analysis (PCA) method. We further apply the Savitzky-Golay filter on the respiration waveform to smoothen it. The respiration rate is finally calculated by performing an auto-correlation operation on the respiration waveform with a window size of 30 s.

5.2 Human Trajectory Tracking

The proposed BFM ratio can also be used to sense macro-motions, such as the trajectory of human walking. The key

(a) Asus RT-AC86U (b) Netgear R7800 (c) Linksys EA8100

(d) Linksys MR9000X (e) TP-LINK WDR7660 (f) TP-LINK WDR7661

Figure 10: All tested routers support MU-MIMO technology.

information we use for human trajectory tracking is the movement speed of the target. Recall that the BFM ratio model has established a quantitative relationship between the BFM-ratio phase change and the dynamic path length change in Section 4.1. By leveraging the geometric relationship between the target and transceivers, we can convert the path length change speed into the radial speed of the target with respect to the transceivers [32]. With another pair of transceivers, we obtain a second radial speed. By fusing the two speeds, we obtain the true target velocity. Note that we assume the initial location of the target is known. Within a short period of time window such as 0.2 s, we can safely assume the target velocity is a constant. We can then calculate the target location after the small time window and iteratively compute the following locations to enable continuous tracking.

6 Evaluation

In this section, we conduct experiments to evaluate the performance of applying the proposed BFM ratio metric to realize two typical sensing applications, i.e., micro-motion respiration monitoring and macro-motion human tracking.

6.1 BFM collection.

We first test the feasibility of BFM data collection on diverse devices and evaluate the performance of sensing using real communication traffic.

BFM data collection on various devices. To demonstrate the generality of our approach, we test six different WiFi routers including Asus RT-AC86U, Netgear R7800, Linksys EA8100, Linksys MR9000X, TP-LINK WDR7660, and TP-LINK WDR7661 as shown in Figure 10. We denote the above routers as R1 $\sim$ R6. Although these routers are of various brands and equipped with different WiFi chips, we are able to successfully collect BFM during the communication process of these routers without changing any firmware or driver. This is because BFM is protocol-compliant feedback information that is available on all the devices that support MU-MIMO.

Sensing under real communication traffic. We also evaluate the performance of respiration monitoring under real

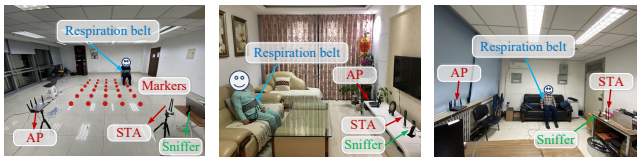

(a) empty room (b) living room (c) office

Figure 11: Three typical environments with different levels of multipath and experiment setup for human respiration sensing.

communication traffic between WiFi AP and STAs. Specifically, we watch live webcasts, listen to music, and browse the web to generate different real-world traffic patterns. In this experiment, we use Asus RT-AC86U as AP and two Tenda U10 cards as the STAs. For different activities, the packet rate varies significantly. When watching live webcasts, the mean sample rate of BFM always exceeds 10 Hz, which is high enough for respiration monitoring. When listening to music and browsing the Web, the BFM comes intermittently and the mean sample rate of BFM is 3 $\sim$ 6 Hz and 3 $\sim$ 4 Hz respectively. For human trajectory tracking, usually a sample rate higher than 20 Hz is required. To trigger more frequent beamforming feedback packets, we use the iperf3 tool [30] to generate UDP traffic from AP to STAs.

6.2 Respiration Monitoring using BFM Ratio

Devices. We employ a Netgear R7800 router equipped with Qualcomm WiFi QCA9984 chipset as the AP and two Tenda U10 as the STAs to collect BFM samples. Our system operates at a central frequency of 5.75 GHz, and the channel bandwidth is 80 MHz. We use a Netgear A6210 as a sniffer to collect feedback packets from the STAs.

Environment. We conduct experiments in an empty room (9.5 m $\times$ 9.8 m), a living room (3.4 m $\times$ 6.1 m) and an office (4.4 m $\times$ 4 m), as shown in Figure 11. In the living room and the office, there are a lot of furniture and electrical appliances which create rich multipath. In the living room, our transceivers are placed at one side of the room, as shown in Figure 11(b). In the office, our transceivers are placed at two sides of the room as shown in Figure 11(c).

Participants. We recruit six volunteers including four males and two females for our experiment, aged between 23 and 57. Throughout the experiment, the user wears a commercial sensor (Neulog Respiration Monitor Belt logger sensor NUL-236 [19]) to obtain ground truth. Their respiration rates range from 12 to 18 bpm (beats per minute).

6.2.1 BFM vs. BFM ratio.

In this section, we compare the performance of respiration monitoring based on BFM and BFM ratio. We let the target breathe naturally at different positions. The positions in the environment are marked with red dots in Figure 11(a).

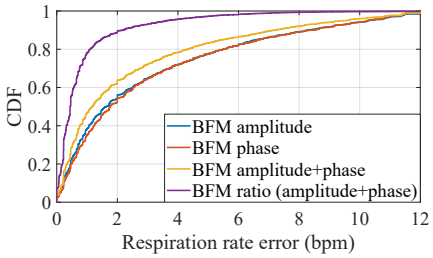

Figure 12: The CDF of respiration sensing error with different signals as input.

Experiment Results. We show the overall respiration rate error and also snapshots of the signal patterns.

- **Respiration rate error.** Figure 12 presents the overall respiration rate errors of different signals. The median errors are 1.61 bpm, 1.76 bpm, 1.17 bpm, and 0.44 bpm for BFM amplitude, BFM phase, BFM amplitude+phase, and BFM ratio, respectively. The errors of using only BFM amplitude or phase are the largest, while using both can only slightly improve the accuracy since the complementary property does not exist. Due to the complementarity of BFM ratio amplitude and phase in respiration monitoring, significantly better performance can be achieved.
- **Breathing induced signal pattern.** Figure 13 presents the detailed patterns of the amplitude and phase of BFM and those of BFM ratio. These signals are filtered by a Savitzky-Golay filter. We can see that while BFM amplitude or phase can be used for respiration monitoring at position 1 and position 2, both of them are too weak to be used at position 3. In comparison, at all three positions, at least one of the BFM ratio amplitude and phase can be utilized for respiration monitoring, outperforming BFM-based method.

6.2.2 Ideal CSI vs. BFM ratio.

To compare the performance with ideal CSI, we use WARP V3 platform [39] to collect CSI data. We deploy the AP and STA with a LoS distance of 2.4 m as shown in Figure 14. We ask a target to sit in the chair located on the perpendicular bisector of the LoS path of the transceivers. We record CSI and BFM data simultaneously when a target breathes naturally. We vary the distance between the target and the LoS path from 2 m to 5 m at a step size of 1 m. Since the sample rates of WARP CSI and BFM are different, we first align the sample rates of these two signals. In addition, the number of subcarriers provided by BFM (234 subcarriers) is larger than that of CSI (56 subcarriers). Here we select the same number of subcarriers (56) for BFM with equal intervals. Then, we feed the amplitude and phase of CSI, and the amplitude and phase of BFM ratio into the method described in Section 5.1 while keeping the other parameters the same.

We plot the mean absolute error (MAE) of respiration rate

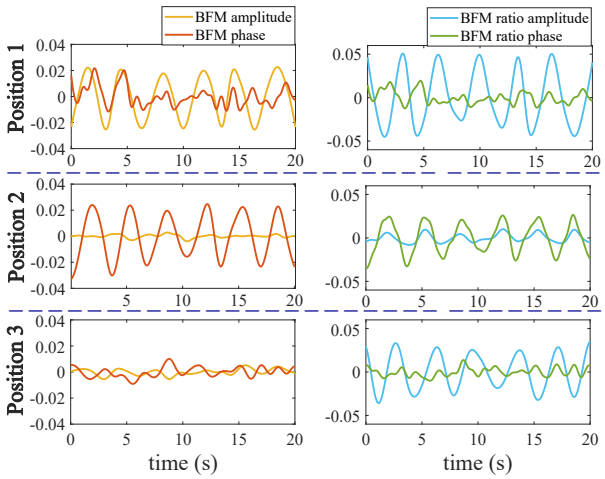

Figure 13: Phase and amplitude patterns of the BFM and BFM ratio when the subject breathes six cycles at three different positions. While BFM amplitude or phase can be used for sensing at Position 1 and 2, neither can be used for sensing at Position 3. In contrast, at least one of the BFM ratio's phase and amplitude can be used for sensing at all locations.

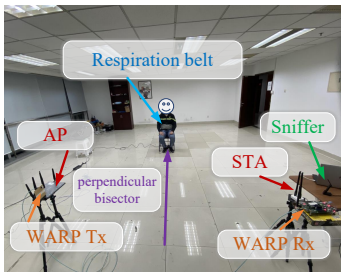

Figure 14: The experiment setup for respiration monitoring. A WARP SDR is used to collect CSI readings for comparison with the BFM-ratio-based method.

with respect to the distance from 2 m to 5 m in Figure 15. The experiment results show that the MAE of respiration monitoring based on BFM ratio is slightly higher than that of CSI. We believe this is mainly because WARP is a high-end software-defined radio platform which allows us to extract cleaner CSI signal. On the other hand, BFM samples extracted from commodity hardware have more noise. Furthermore, since BFM is obtained from CSI through a series of steps including singular value decomposition and compression, there can be a precision loss during the process. Despite that, BFM ratio can still achieve reliable human respiration sensing. We believe that the sensing accuracy can be further improved through signal enhancement algorithms leveraging data from multiple subcarriers [27].

6.2.3 Impact of device and environment diversity

Device diversity. We keep the same environment setting and collect BFM with different routers placed at the same location one by one as shown in Figure 10. We compare the archived MAE for respiration rate monitoring. Despite differ-

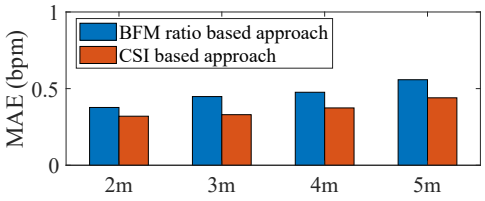

Figure 15: The respiration rate error of CSI-based and BFM-ratio-based approaches at different distances.

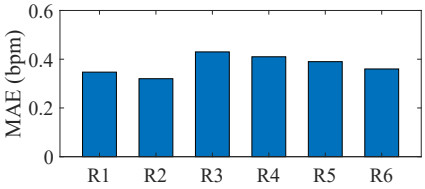

Figure 16: The respiration rate error of different devices.

ent numbers of antennas equipped, similar MAEs are achieved at different devices as illustrated in Figure 16. The results demonstrate that the proposed BFM sensing can be realized on a large range of WiFi devices.

Environment diversity. We deploy AP and STAs in two other rooms with rich multipath as shown in Figure 11(b) and Figure 11(c). The achieved MAEs for respiration rate sensing are 0.43 bpm and 0.46 bpm respectively, which are comparable to that in the empty room.

Through-wall deployment. We further conduct experiments under the following through-wall deployments. AP and sniffer are in the same room while STAs and the target are in another room. The MAE of respiration rate is 0.76 bpm. Compared to the previous experiment where all devices are in the same room, the dynamic path is now attenuated, which leads to a decrease of the signal fluctuation caused by respiration. The error is now larger but still below 1 bpm. Note that the location of the sniffer does not matter as long as it can overhear the CBF packets containing BFM information.

Multi-target scenario. In this subsection, we test the capability of multi-target respiration monitoring. We consider three typical cases as shown in Figure 18. For MU-MIMO transmission, at least two WiFi stations need to be involved so we consider two WiFi stations in these cases.

- Case 1: Two targets are in the same room and the two targets are close to each other.
- Case 2: Two targets are in the same room but are separated from each other with an 8 m distance in between.
- Case 3: Two targets are in different rooms.

In multi-target scenarios, signals reflected from multiple targets are superimposed. When the distance between targets is close (Case 1), signals from multiple targets can not be easily separated in the time domain or spatial domain. We exploit the independence of breathing patterns between targets and apply the blind source separation method [60] to obtain

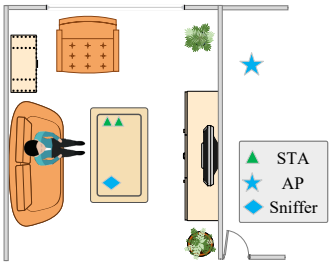

Figure 17: A through-wall deployment for respiration sensing.

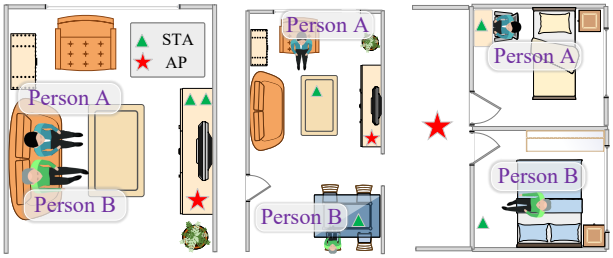

(a) Case 1 (b) Case 2 (c) Case 3

Figure 18: Experiment environments and setup for multi-target respiration sensing.

each target's breathing information. In our experiment, with BFM ratio as the input, a low MAE of 0.53 bpm can be achieved. For Cases 2 and 3, the targets are separated by a large distance or a wall. Each STA's signal variation is more affected by the nearer target. The respiration rate of each target can thus be directly estimated from the BFM ratio variation of each STA. The MAEs of the estimated respiration rates in the two cases are 0.44 bpm and 0.38 bpm, respectively. These achieved low MAEs show that BFM ratio can support accurate multi-target respiration monitoring.

6.3 Human Tracking using BFM ratio

In this section, we evaluate the performance of applying BFM-ratio for velocity estimation to support human tracking.

6.3.1 Experiment setup

We conduct experiments in two typical indoor environments, i.e., an empty room (9.5 m $\times$ 9.8 m), as shown in Figure 19(a), and a meeting room (6.4 m $\times$ 6.4 m), as shown in Figure 19(b). One WiFi AP (Netgear R7800) and two STAs (Tenda U10) are mounted on tripods at a height of one meter. We place two STAs at different locations to make the two AP-STA lines perpendicular to each other. The LoS distance between the transmitter and receivers is set as 4.2 m. Three volunteers (2 men and 1 woman) are recruited to participate in the experiments. The participants are asked to walk naturally along ten trajectories of various shapes, including straight line, diamond, rectangle, triangle and 'N' path. Each volunteer walks along each trajectory 20 times.

6.3.2 Performance of human tracking

We plot the recovered human walking trajectories and the ground truth trajectories (GTT) in Figure 20. We can see

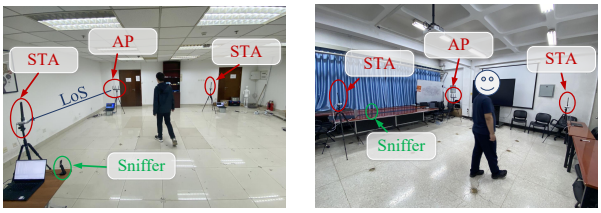

(a) empty room (b) meeting room

Figure 19: The experiment setup for human trajectory tracking in two different environments.

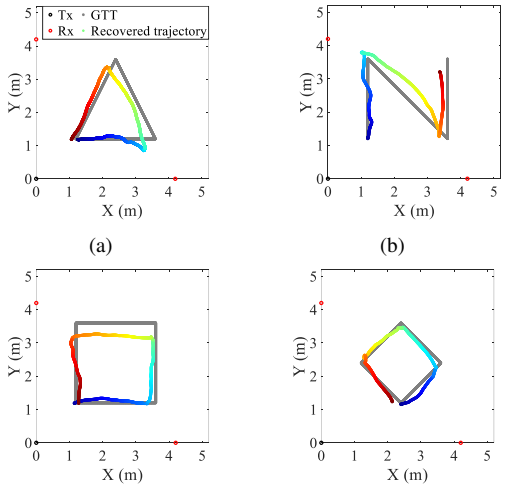

Figure 20: Human trajectory tracking results with BFM ratio.

that with just two STAs, we can achieve accurate human trajectory tracking with commodity WiFi. We present the tracking error in Figure 21. The median localization error is 0.43 m and 0.72 m in the empty room and in the meeting room, respectively. This result shows that BFM ratio can be used to not just detect motion but also quantitatively measure the motion displacement.

6.3.3 Performance in the challenging real-life scenario

In order to demonstrate the performance of BFM ratio tracking in real environments with rich multipath and NLoS, we conduct additional experiments in a living room as shown in Figure 22(a). The size of the room is 3.4 $m \times 6.1$ m, and most of the space is filled with furniture, including sofas, coffee table, and TV cabinet. AP and one STA are placed near the wall. The other STA is placed in the adjacent room with a wall of 30 cm thickness. The straight-line distances between two STAs and AP are 4 m. The target starts walking from a corner near the coffee table and stops at the TV cabinet. We ask the participant to walk along this trajectory 20 times. An example of the trajectory estimate is shown in Figure 22(b) which matches the ground truth. The median localization error is 0.98 m as shown in Figure 21. Due to richer multipaths, the tracking error in the living room is larger than those in the empty room and meeting room.

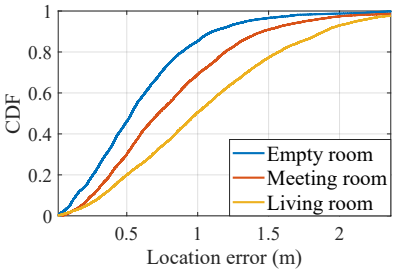

Figure 21: CDF plot of the localization error.

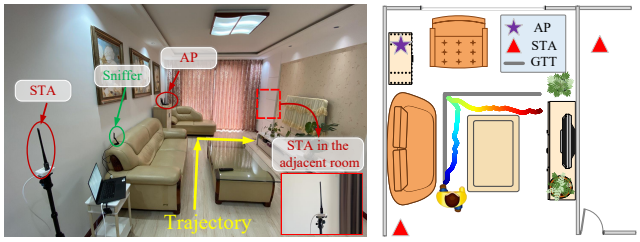

(a) Living room with rich multipath (b) The estimated trajectory

Figure 22: Human trajectory tracking in a multipath-rich and NLoS environment.

7 Related work

In this section, we briefly review the most related work.

7.1 WiFi based contactless sensing

Due to easy access of RSSI at most WiFi devices, in the early years, human sensing was mainly based on RSSI readings. RSSI was used for human respiration monitoring [1] and also for fingerprinting-based localization [59]. However, as RSSI only contains signal strength information, the performance is relatively coarse.

In 2010, some open source CSI tools [17] were developed to support extracting CSI from several 802.11n WiFi chips. Since then, CSI-based sensing has drawn widespread attention in both academia and industry. Promising progress has been achieved from coarse-grained fall detection [42, 46], gesture recognition [15, 38, 40], activity recognition [33, 56], indoor tracking [25, 36, 51] to fine-grained vital sign monitoring [61, 67]. Compared to RSSI, CSI contains both amplitude and phase information. Richer target context such as speed and angle can be obtained from CSI data. A lot of models were developed based on CSI input including CSI-speed model [44], Fresnel zone model [41, 52], Angle-of-Arrival model [26] and CSI-ratio model [62]. CSI-based sensing requires specially tailored WiFi firmware and CSI tools to extract CSI samples. It thus only works with very few WiFi cards such as Intel 5300 and Atheros 9x series cards.

On the other hand, BFM can be extracted from a large range of WiFi devices without the need of hacking WiFi firmware or drivers. It is thus promising to utilize BFM for WiFi sensing. There has been some initial exploration of BFM sensing. In a recent work [20], the authors observed that BFM amplitude is

affected by human respiration and respiration rate can be monitored using BFM. Another recent work [21] further showed that the number of repetitive activities can be counted using BFM phase information. However, these initial studies are empirical research based on experiment observations. There is no theoretical analysis to help people fully understand the underlying mechanism and also the relationship between CSI and BFM. In this work, we lay the theoretical foundation for BFM sensing and analyze the sensing capabilities of BFM. A recent work (BeamSense [49]) proposed to recover CSI from BFM for sensing. To recover BFM from CSI, BeamSense required to extract both downlink BFM and uplink BFM. While downlink BFM can be easily extracted, uplink BFM can only be extracted from 1% WiFi stations, which is acknowledged in BeamSense. In contrast, downlink CBF alone is enough for our proposed system to work.

7.2 Other RF-based sensing

In addition to WiFi signals, a wide range of wireless technologies such as RFID, LoRa, FMCW radar, and IR-UWB radar, have been used for sensing. RFID is a technology that locates and identifies tags attached to items using radio waves. RFID has been utilized to realize sensing applications including localization [28], authentication [12], human activity recognition [58], gesture recognition [70] and material sensing [43, 53]. LoRa is a low-power, long-distance wireless technology designed for connections between IoT devices. LoRa is also utilized for contactless sensing applications such as localization [18], human detection [11], respiration monitoring [63] and human tracking [54, 63]. Recent works further applied LoRa signals for multi-target sensing [65] and soil moisture monitoring [10]. FMCW and IR-UWB radars are two commonly used radars for contactless sensing. They have been used for vital sign monitoring [5, 16, 64, 66], human tracking [2, 3, 13, 69], and even emotion recognition [68]. While the above technologies showed promising results in various sensing applications, they still require dedicated devices that are not yet widely used in our daily life.

8 Discussion

Privacy concern. Since BFM is not encrypted, anyone including attackers can eavesdrop on the BFM transmissions and use the captured BFM readings to sniff human contexts such as location and activities. One potential solution is to apply random offsets (both amplitude and phase offsets) to each element of the BFM readings to corrupt the quantitative relationship between BFM ratio and target motion. However, this method does affect the communication function of BFM. We thus need to embed the random offsets in the encrypted WiFi packets to compensate the applied offsets at legitimate nodes. This will unavoidably lead to more complicated protocol design and higher computational load which eventually may degrade the throughput performance. We believe protecting targets from being sensed by BFM readings is an exciting topic worth more effort.

AoA and ToF estimation from BFM. The key information to enable AoA estimation is the signal phase readings, more precisely, the phase difference between antennas. Since BFM preserves the phase difference between antennas during the compression process, the steering vector can still be constructed for AoA estimation. BFM may have difficulties being used for ToF estimation. This is because the phase relationship between sub-carriers is the key information for ToF estimates. During the compression process, the phase readings subtracted at different subcarriers are different, corrupting the phase relationship between subcarriers which is critical for ToF estimation.

CSI vs. BFM. We believe few manufacturers are willing to release the raw CSI readings to the public and we do not expect a change in the near future. There are two main reasons for this. The first reason is that due to the high sampling rate and detailed information on each subcarrier, the high transmission cost of CSI (i.e., a large amount of data) can degrade the communication throughput. Second, detailed CSI information can also leak confidential chip performance information to the public. This is why BFM adopts a lower sampling rate and only transmits compressed partial data. Therefore, compared to CSI, we believe BFM is the choice for real-world adoption of WiFi sensing. We believe building the theoretical foundation for BFM-based sensing moves a big step towards real-world adoption of WiFi sensing.

9 Conclusion

While WiFi CSI sensing has been popular in the past decade, CSI can only be extracted from very few WiFi cards, greatly hindering the adoption of CSI-based WiFi sensing. We observe an exciting opportunity brought by the new-generation WiFi devices supporting 802.11ac MU-MIMO technology, i.e., a new channel information called BFM can be extracted from a large range of WiFi cards for sensing. In this paper, we studied the underlying principle of BFM sensing by revealing the relationship between BFM and CSI. We propose to take the ratio of two BFM elements to avoid the inherent issues associated with BFM for sensing. The theoretical analysis lays a foundation for WiFi sensing on new-generation WiFi devices. Comprehensive experiments demonstrated the effectiveness of applying BFM for fine-grained sensing.

Acknowledgments

This research is supported by NSFC A3 Project (No. 62061146001), PKU-NTU Collaboration Project, China Postdoctoral Science Foundation (No. 2021TQ0048), Beijing Nova Program (20220484138), Beijing Natural Science Foundation (L223034), National Natural Science Foundation of China (No. 62172394), and Youth Innovation Promotion Association, Chinese Academy of Sciences (No. 2020109).

References

[1] Heba Abdelnasser, Khaled A Harras, and Moustafa Youssef. UbiBreathe: A ubiquitous non-invasive WiFi-based breathing estimator. In *Proceedings of the 16th ACM International Symposium on Mobile Ad Hoc Networking and Computing*, pages 277–286, 2015.

[2] Fadel Adib, Zach Kabelac, Dina Katabi, and Robert C Miller. 3d tracking via body radio reflections. In *11th USENIX Symposium on Networked Systems Design and Implementation (NSDI 14)*, pages 317–329, 2014.

[3] Fadel Adib, Zachary Kabelac, and Dina Katabi. Multi-person localization via rf body reflections. In *12th USENIX Symposium on Networked Systems Design and Implementation (NSDI 15)*, pages 279–292, 2015.

[4] Fadel Adib and Dina Katabi. See through walls with WiFi! In *Proceedings of the ACM SIGCOMM 2013 conference on SIGCOMM*, pages 75–86, 2013.

[5] Fadel Adib, Hongzi Mao, Zachary Kabelac, Dina Katabi, and Robert C Miller. Smart homes that monitor breathing and heart rate. In *Proceedings of the 33rd annual ACM conference on human factors in computing systems*, pages 837–846, 2015.

[6] Andreas Anderhub and Zac Wilson. Centrifi: A centralizedwireless access point management platform. 2020.

[7] Douglas N Arnold and Jonathan P Rogness. Möbius transformations revealed. *Notices of the American Mathematical Society*, 55(10):1226–1231, 2008.

[8] Apurv Bhartia, Bo Chen, Feng Wang, Derrick Pallas, Raluca Musaloiu-E, Ted Tsung-Te Lai, and Hao Ma. Measurement-based, practical techniques to improve 802.11ac performance. In *Proceedings of the 2017 Internet Measurement Conference*, IMC '17, page 205–219, New York, NY, USA, 2017. Association for Computing Machinery.

[9] Wireless CAT. "TP-LINK TL-XDR6060", [online]. https://wikidevi.wi-cat.ru/TP-LINK_TL-XDR6060.

[10] Zhaoxin Chang, Fusang Zhang, Jie Xiong, Junqi Ma, Beihong Jin, and Daqing Zhang. Sensor-free soil moisture sensing using lora signals. *Proceedings of the ACM on Interactive, Mobile, Wearable and Ubiquitous Technologies*, 6(2):1–27, 2022.

[11] Lili Chen, Jie Xiong, Xiaojiang Chen, Sunghoon Ivan Lee, Kai Chen, Dianhe Han, Dingyi Fang, Zhanyong Tang, and Zheng Wang. Widesee: Towards wide-area contactless wireless sensing. In *Proceedings of the 17th Conference on Embedded Networked Sensor Systems*, pages 258–270, 2019.

[12] Xingyu Chen, Jia Liu, Xia Wang, Haisong Liu, Dong Jiang, and Lijun Chen. Eingerprint: Robust energy-related fingerprinting for passive RFID tags. In *17th USENIX Symposium on Networked Systems Design and Implementation (NSDI 20)*, pages 1101–1113, Santa Clara, CA, February 2020. USENIX Association.

[13] Zhe Chen, Chao Cai, Tianyue Zheng, Jun Luo, Jie Xiong, and Xin Wang. Rf-based human activity recognition using signal adapted convolutional neural network. *IEEE Transactions on Mobile Computing*, 22(1):487–499, 2021.

[14] IEEE Computer Society LAN/MAN Standards Committee et al. Ieee standard for information technology—telecommunications and information exchange between systems local and metropolitan area networks—specific requirements - part 11: Wireless lan medium access control (mac) and physical layer (phy) specifications. *IEEE Std 802.11-2016 (Revision of IEEE Std 802.11-2012)*, pages 1–3534, 2016.

[15] Ruiyang Gao, Wenwei Li, Yaxiong Xie, Enze Yi, Leye Wang, Dan Wu, and Daqing Zhang. Towards robust gesture recognition by characterizing the sensing quality of wifi signals. *Proceedings of the ACM on Interactive, Mobile, Wearable and Ubiquitous Technologies*, 6(1):1–26, 2022.

[16] Unsoo Ha, Salah Assana, and Fadel Adib. Contactless seismocardiography via deep learning radars. In *Proceedings of the 26th Annual International Conference on Mobile Computing and Networking*, pages 1–14, 2020.

[17] Daniel Halperin, Wenjun Hu, Anmol Sheth, and David Wetherall. Tool release: Gathering 802.11n traces with channel state information. *ACM SIGCOMM CCR*, 41(1):53, Jan. 2011.

[18] Bashima Islam, Md Tamzeed Islam, and Shahriar Nirjon. Feasibility of lora for indoor localization. *Appl. Sci*, 2017:8565550, 2017.

[19] Wern Kam, Waleed Soliman Mohammed, Gabriel Leen, Mary O'Keeffe, Kieran O'Sullivan, Sinead O'Keeffe, and Elfed Lewis. Compact and low-cost optical fiber respiratory monitoring sensor based on intensity interrogation. *Journal of Lightwave Technology*, 35(20):4567–4573, 2017.

[20] Takamochi Kanda, Takashi Sato, Hiromitsu Awano, Sota Kondo, and Koji Yamamoto. Respiratory rate estimation based on wifi frame capture. In *2022 IEEE 19th Annual Consumer Communications & Networking Conference (CCNC)*, pages 881–884. IEEE, 2022.

[21] Sorachi Kato, Tomoki Murakami, Takuya Fujihashi, Takashi Watanabe, and Shunsuke Saruwatari. Cbr-ace: Counting human exercise using wi-fi beamforming reports. *Journal of Information Processing*, 30:66–74, 2022.

[22] Simon Kaufmann. Sharing is caring: Throughput fairness in virtual wireless lans.

[23] Joonsuk Kim and Inkyu Lee. 802.11 wlan: history and new enabling mimo techniques for next generation standards. *IEEE Communications Magazine*, 53(3):134–140, 2015.

[24] Vladimir V Kisil. *Geometry of Möbius Transformations*. IMPERIAL COLLEGE PRESS, 2012.

[25] Manikanta Kotaru, Kiran Joshi, Dinesh Bharadia, and Sachin Katti. Spotfi: Decimeter level localization using wifi. In *Proceedings of the 2015 ACM Conference on Special Interest Group on Data Communication*, pages 269–282, 2015.

[26] Xiang Li, Shengjie Li, Daqing Zhang, Jie Xiong, Yasha Wang, and Hong Mei. Dynamic-music: accurate device-free indoor localization. In *Proceedings of the 2016 ACM international joint conference on pervasive and ubiquitous computing*, pages 196–207, 2016.

[27] Yang Li, Dan Wu, Jie Zhang, Xuhai Xu, Yaxiong Xie, Tao Gu, and Daqing Zhang. Diversense: Maximizing wi-fi sensing range leveraging signal diversity. *Proceedings of the ACM on Interactive, Mobile, Wearable and Ubiquitous Technologies*, 6(2):1–28, 2022.

[28] Bo Liang, Purui Wang, Renjie Zhao, Heyu Guo, Pengyu Zhang, Junchen Guo, Shunmin Zhu, Hongqiang Harry Liu, Xinyu Zhang, and Chenren Xu. RF-Chord: Towards deployable RFID localization system for logistic networks. In *20th USENIX Symposium on Networked Systems Design and Implementation (NSDI 23)*, pages 1783–1799, Boston, MA, April 2023. USENIX Association.

[29] C Lowanichkiattikul, M Dhanachai, C Sitathanee, S Khachonkham, and P Khaothong. Impact of chest wall motion caused by respiration in adjuvant radiotherapy for postoperative breast cancer patients. *SpringerPlus*, 5:1–8, 2016.

[30] Bruce Mah, Jon Dugan, Brian Tierney, Jef Poskanzer, and Seth Elliot. iperf, version 3, [online]. https://iperf.fr.

[31] Pedro Melgarejo, Xinyu Zhang, Parameswaran Ramanathan, and David Chu. Leveraging directional antenna capabilities for fine-grained gesture recognition. In *Proceedings of the 2014 ACM International Joint Conference on pervasive and ubiquitous computing*, pages 541–551, 2014.

[32] Kai Niu, Xuanzhi Wang, Fusang Zhang, Rong Zheng, Zhiyun Yao, and Daqing Zhang. Rethinking doppler effect for accurate velocity estimation with commodity wifi devices. *IEEE Journal on Selected Areas in Communications*, 2022.

[33] Sameera Palipana, David Rojas, Piyush Agrawal, and Dirk Pesch. FallDeFi: Ubiquitous fall detection using commodity Wi-Fi devices. *Proceedings of the ACM on Interactive, Mobile, Wearable and Ubiquitous Technologies*, 1(4):1–25, 2018.

[34] Eldad Perahia and Robert Stacey. *Next Generation Wireless LANs: Throughput, Robustness, and Reliability in 802*. Cambridge Univ. Press, 2008.

[35] Qifan Pu, Sidhant Gupta, Shyamnath Gollakota, and Shwetak Patel. Whole-home gesture recognition using wireless signals. In *Proceedings of the 19th annual international conference on Mobile computing & networking*, pages 27–38, 2013.

[36] Kun Qian, Chenshu Wu, Yi Zhang, Guidong Zhang, Zheng Yang, and Yunhao Liu. Widar2. 0: Passive human tracking with a single wi-fi link. In *Proceedings of the 16th Annual International Conference on Mobile Systems, Applications, and Services*, pages 350–361, 2018.

[37] H Schwerdtfeger. Geometry of complex numbers: Circle geometry moebius transformation. 1979.

[38] Sheng Tan and Jie Yang. Wifinger: Leveraging commodity wifi for fine-grained finger gesture recognition. In *Proceedings of the 17th ACM international symposium on mobile ad hoc networking and computing*, pages 201–210, 2016.

[39] Rice University. "warp project", [Online]. http://warp.rice.edu.

[40] Raghav H Venkatnarayan, Griffin Page, and Muhammad Shahzad. Multi-user gesture recognition using wifi. In *Proceedings of the 16th Annual International Conference on Mobile Systems, Applications, and Services*, pages 401–413, 2018.

[41] Hao Wang, Daqing Zhang, Junyi Ma, Yasha Wang, Yuxiang Wang, Dan Wu, Tao Gu, and Bing Xie. Human respiration detection with commodity wifi devices: do user location and body orientation matter? In *Proceedings of the 2016 ACM International Joint Conference on Pervasive and Ubiquitous Computing*, pages 25–36, 2016.

[42] Hao Wang, Daqing Zhang, Yasha Wang, Junyi Ma, Yuxiang Wang, and Shengjie Li. Rt-fall: A real-time and contactless fall detection system with commodity wifi devices. *IEEE Transactions on Mobile Computing*, 16(2):511–526, 2017.

[43] Ju Wang, Jie Xiong, Xiaojiang Chen, Hongbo Jiang, Rajesh Krishna Balan, and Dingyi Fang. Tagscan: Simultaneous target imaging and material identification with commodity rfid devices. In *Proceedings of the 23rd Annual International Conference on Mobile Computing and Networking*, pages 288–300, 2017.

[44] Wei Wang, Alex X Liu, Muhammad Shahzad, Kang Ling, and Sanglu Lu. Understanding and modeling of wifi signal based human activity recognition. In *Proceedings of the 21st annual international conference on mobile computing and networking*, pages 65–76, 2015.

[45] Yan Wang, Jian Liu, Yingying Chen, Marco Gruteser, Jie Yang, and Hongbo Liu. E-eyes: device-free location-oriented activity identification using fine-grained wifi signatures. In *Proceedings of the 20th annual international conference on Mobile computing and networking*, pages 617–628, 2014.

[46] Yuxi Wang, Kaishun Wu, and Lionel M. Ni. Wifall: Device-free fall detection by wireless networks. *IEEE Transactions on Mobile Computing*, 16(2):581–594, 2017.

[47] Wikipedia. "ieee_802.11ac-2013", [online]. https://en.wikipedia.org/wiki/IEEE_802.11ac-2013.

[48] Joey Wilson and Neal Patwari. See-through walls: Motion tracking using variance-based radio tomography networks. *IEEE Transactions on Mobile Computing*, 10(5):612–621, 2010.

[49] Chenhao Wu, Xuan Huang, Jun Huang, and Guoliang Xing. Enabling ubiquitous wifi sensing with beamforming reports. In *Proceedings of the ACM SIGCOMM 2023 Conference*, ACM SIGCOMM '23, page 20–32, New York, NY, USA, 2023. Association for Computing Machinery.

[50] Dan Wu, Ruiyang Gao, Youwei Zeng, Jinyi Liu, Leye Wang, Tao Gu, and Daqing Zhang. Fingerdraw: Sub-wavelength level finger motion tracking with wifi signals. *Proceedings of the ACM on Interactive, Mobile, Wearable and Ubiquitous Technologies*, 4(1):1–27, 2020.

[51] Dan Wu, Youwei Zeng, Ruiyang Gao, Shengjie Li, Yang Li, Rahul C Shah, Hong Lu, and Daqing Zhang. Witraj: robust indoor motion tracking with wifi signals. *IEEE Transactions on Mobile Computing*, 2021.

[52] Dan Wu, Daqing Zhang, Chenren Xu, Yasha Wang, and Hao Wang. Widir: Walking direction estimation using wireless signals. In *Proceedings of the 2016 ACM International Joint Conference on Pervasive and Ubiquitous Computing*, UbiComp '16, page 351–362, New York, NY, USA, 2016. Association for Computing Machinery.

[53] Binbin Xie, Jie Xiong, Xiaojiang Chen, Eugene Chai, Liyao Li, Zhanyong Tang, and Dingyi Fang. Tagtag: material sensing with commodity rfid. In *Proceedings of the 17th conference on embedded networked sensor systems*, pages 338–350, 2019.

[54] Binbin Xie, Yuqing Yin, and Jie Xiong. Pushing the limits of long range wireless sensing with lora. *Proc. ACM Interact. Mob. Wearable Ubiquitous Technol.*, 5(3), sep 2021.

[55] Yaxiong Xie, Zhenjiang Li, and Mo Li. Precise power delay profiling with commodity wifi. In *Proceedings of the 21st Annual International Conference on Mobile Computing and Networking*, MobiCom '15, page 53–64, New York, NY, USA, 2015. ACM.

[56] Yang Xu, Wei Yang, Jianxin Wang, Xing Zhou, Hong Li, and Liusheng Huang. Wistep: Device-free step counting with wifi signals. *Proceedings of the ACM on Interactive, Mobile, Wearable and Ubiquitous Technologies*, 1(4):1–23, 2018.

[57] Zheng Yang, Zimu Zhou, and Yunhao Liu. From RSSI to CSI: Indoor localization via channel response. *ACM Computing Surveys (CSUR)*, 46(2):1–32, 2013.

[58] Lina Yao, Quan Z. Sheng, Xue Li, Tao Gu, Mingkui Tan, Xianzhi Wang, Sen Wang, and Wenjie Ruan. Compressive representation for device-free activity recognition with passive rfid signal strength. *IEEE Transactions on Mobile Computing*, 17(2):293–306, 2018.

[59] Moustafa Youssef, Matthew Mah, and Ashok Agrawala. Challenges: device-free passive localization for wireless environments. In *Proceedings of the 13th annual ACM international conference on Mobile computing and networking*, pages 222–229, 2007.

[60] Vicente Zarzoso and Pierre Comon. Robust independent component analysis by iterative maximization of the kurtosis contrast with algebraic optimal step size. *IEEE Transactions on neural networks*, 21(2):248–261, 2009.

[61] Youwei Zeng, Dan Wu, Ruiyang Gao, Tao Gu, and Daqing Zhang. FullBreathe: Full human respiration detection exploiting complementarity of CSI phase and amplitude of WiFi signals. *Proceedings of the ACM on Interactive, Mobile, Wearable and Ubiquitous Technologies*, 2(3):1–19, 2018.

[62] Youwei Zeng, Dan Wu, Jie Xiong, Enze Yi, Ruiyang Gao, and Daqing Zhang. Farsense: Pushing the range limit of wifi-based respiration sensing with csi ratio of two antennas. *Proceedings of the ACM on Interactive, Mobile, Wearable and Ubiquitous Technologies*, 3(3):1–26, 2019.

[63] Fusang Zhang, Zhaoxin Chang, Kai Niu, Jie Xiong, Beihong Jin, Qin Lv, and Daqing Zhang. Exploring lora for long-range through-wall sensing. *Proc. ACM Interact. Mob. Wearable Ubiquitous Technol.*, 4(2), jun 2020.

[64] Fusang Zhang, Zhaoxin Chang, Jie Xiong, Junqi Ma, Jiazhi Ni, Wenbo Zhang, Beihong Jin, and Daqing Zhang. Embracing consumer-level uwb-equipped devices for fine-grained wireless sensing. 6(4), jan 2023.

[65] Fusang Zhang, Zhaoxin Chang, Jie Xiong, Rong Zheng, Junqi Ma, Kai Niu, Beihong Jin, and Daqing Zhang. Unlocking the beamforming potential of lora for long-range multi-target respiration sensing. *Proc. ACM Interact. Mob. Wearable Ubiquitous Technol.*, 5(2), jun 2021.

[66] Fusang Zhang, Jie Xiong, Zhaoxin Chang, Junqi Ma, and Daqing Zhang. Mobi2sense: Empowering wireless sensing with mobility. In *Proceedings of the 28th Annual International Conference on Mobile Computing And Networking*, MobiCom '22, page 268–281, New York, NY, USA, 2022. Association for Computing Machinery.

[67] Fusang Zhang, Daqing Zhang, Jie Xiong, Hao Wang, Kai Niu, Beihong Jin, and Yuxiang Wang. From Fresnel Diffraction Model to Fine-grained Human Respiration Sensing with Commodity Wi-Fi Devices. *Proceedings of the ACM on Interactive, Mobile, Wearable and Ubiquitous Technologies*, 2(1):1–23, 2018.

[68] Mingmin Zhao, Fadel Adib, and Dina Katabi. Emotion recognition using wireless signals. In *Proceedings of the 22nd annual international conference on mobile computing and networking*, pages 95–108, 2016.

[69] Mingmin Zhao, Yonglong Tian, Hang Zhao, Mohammad Abu Alsheikh, Tianhong Li, Rumen Hristov, Zachary Kabelac, Dina Katabi, and Antonio Torralba. Rf-based 3d skeletons. In *Proceedings of the 2018 Conference of the ACM Special Interest Group on Data Communication*, pages 267–281, 2018.

[70] Yongpan Zou, Jiang Xiao, Jinsong Han, Kaishun Wu, Yun Li, and Lionel M. Ni. Grfid: A device-free rfid-based gesture recognition system. *IEEE Transactions on Mobile Computing*, 16(2):381–393, 2017.